ROYAL SOCIETY OPEN SCIENCE

rsos.royalsocietypublishing.org

Research

**Cite this article:** Hou L, Yu Q, Wang K, Qin Q, Wei M, Yang F. 2018 Oxidation kinetics of $YBaCo_4O_{7+\delta}$ and substituted oxygen carriers. *R. Soc. open sci.* **5**: 180150.
http://dx.doi.org/10.1098/rsos.180150

Received: 1 February 2018
Accepted: 2 May 2018

**Subject Category:**
Chemistry

**Subject Areas:**
energy/thermodynamics

**Keywords:**
oxidation, kinetics, low temperature, oxygen carriers

**Author for correspondence:**
Qingbo Yu
e-mail: yuqb@smm.neu.edu.cn

This article has been edited by the Royal Society of Chemistry, including the commissioning, peer review process and editorial aspects up to the point of acceptance.

Electronic supplementary material is available online at https://dx.doi.org/10.6084/m9.figshare.c.4114535.

THE ROYAL SOCIETY PUBLISHING

# Oxidation kinetics of $YBaCo_4O_{7+\delta}$ and substituted oxygen carriers

Limin Hou, Qingbo Yu, Kun Wang, Qin Qin, Mengqi Wei and Fan Yang

School of Metallurgy, Northeastern University, No. 11, Lane 3, Wenhua Road, He Ping District, Shenyang 110819, Liaoning, People's Republic of China

LH, 0000-0002-4077-8541

In this paper, the relaxation kinetics of the oxidation process of the $YBaCo_4O_{7+\delta}$, $Y_{0.95}Ti_{0.05}BaCo_4O_{7+\delta}$ and $Y_{0.5}Dy_{0.5}BaCo_4O_{7+\delta}$ oxygen carriers is studied with isothermal reaction data. XRD analysis for fresh samples shows that all the samples have $YBaCo_4O_{7+\delta}$ structure. Scanning electron microscopy images of samples show that the samples consist of porous agglomerates of primary particles. Isothermal TG experiments are conducted with temperatures of 290°C, 310°C, 330°C and 350°C, respectively. It is found that the Avrami-Erofeev model describes solid-phase changes in the oxygen absorption process adequately. The results show that the distributed activation energies of the oxidation process obtained by the Avrami-Erofeev model are 42.079 kJ mol$^{-1}$, 42.944 kJ mol$^{-1}$ and 41.711 kJ mol$^{-1}$ for the $YBaCo_4O_{7+\delta}$, $Y_{0.95}Ti_{0.05}BaCo_4O_{7+\delta}$ and $Y_{0.5}Dy_{0.5}BaCo_4O_{7+\delta}$ oxygen carriers, respectively. The kinetic model was obtained to predict the oxygen carrier conversion of oxygen absorption for different time durations. The kinetic parameters obtained here are quite vital when this material is used in reactors.

## 1. Introduction

It is generally accepted that carbon dioxide ($CO_2$) emission is the main contributor to global warming. Oxygen-enriched combustion, one of the possible options to reduce $CO_2$ emission, is not applied widely in industry due to the high cost of oxygen production. The process of chemical looping air separation (CLAS) was developed by Moghtaderi & Song in 2010 [1]. The process saves 74% of the power of the cryogenic air separation process [1]. The schematic of the CLAS process is described elsewhere [2]. The oxygen carrier circulates between the oxidation reactor and the reduction reactor. In the oxidation reactor, the oxygen carrier is fully oxidized by oxygen. In the reduction reactor, the oxygen carrier is fully reduced by steam or $CO_2$.

Oxygen carrier materials are mainly those of metal oxide, perovskite and sulfate. The metal oxide oxygen carriers such as those that are Cu-based, Co-based and Mn-based have attracted the interest of researchers [3–13]. Perovskite oxygen carriers such as $Ca_{1-x}Pr_xMnO_{3-\delta}$, $SrCoFe_{3-\delta}$ and $LaFe_{1-x}Mn_xO_3$ also have been investigated [14–16]. Zhao *et al*. [15] found that Mn substitution in $LaFeO_3$ not only was conducive to the partial oxidation of $CH_4$, but also enhanced the lattice oxygen mobility from the bulk to the surface of the oxygen carrier. Because of a low melting point and serious agglomeration of metal oxide, various support materials such as $ZrO_2$, $TiO_2$ and $SiO_2$ have been explored [11,17,18]. Wang *et al*. [19] reported that the reduction rate of the combined $CuO/Mn_2O_3$ oxygen carrier with $ZrO_2$ as a binder increased with increasing reduction temperature. Wang *et al*. [20] found that the $Fe_2O_3$ oxygen carrier had an effective impact on the conversion of typical bituminous coal in a chemical looping combustion system. Whitty & Clayton [21] reported that the activation energy of the oxidation of the CuO oxygen carrier with $ZrO_2$ as a binder was 202 kJ mol$^{-1}$. Arjmand *et al*. [12] found that the activation energy of reduction reaction of the CuO oxygen carrier was 313 kJ mol$^{-1}$. Hossain found that the reduction kinetics of the NiO/Ce-$\gamma Al_2O_3$ oxygen carriers was favourably expressed by the nucleation and crystal growth model. The estimated energy of activation for the reduction process was found to be in the range of 52–55 kJ mol$^{-1}$ [22]. Zhu *et al*. found that the reduction characteristics of oxygen carriers of $Fe_2O_3$–60 wt%/$Al_2O_3$ had an impact on the efficiency of the chemical looping hydrogen generation process. $Fe_3O_4$–FeO was determined as the rate-limiting step with a lower reaction rate constant and a higher activation energy [23]. Hossain & de Lasa [24] found that the nucleation and nuclei growth model provided a better description of the reduction process for CoO–NiO/$\alpha Al_2O_3$ oxygen carriers. Li *et al*. [25] found that a moving-bed reducer showed better performance than a fluidized-bed reducer for the syngas chemical looping process.

There has been extensive reporting in the literature on metallic oxides; unfortunately, industrial applications of metallic oxides consume a large amount of energy as their reaction temperatures are high. Hence investigations with oxygen carriers, which can react at low temperatures and are extremely time-efficient. It is excellent that the waste heat of low temperatures can be used as heat resources as the waste heat resources have not been used effectively. $YBaCo_4O_{7+\delta}$ (donated Y114 phase) was synthesized originally by Valldor & Andersson in 2002 [26]. Karppinen *et al.* reported that $YBaCo_4O_{7+\delta}$ experienced two processes: oxygen intake and release (the first being around 200–400°C, the other around 600–900°C) when heated to 1100°C in an oxygen-containing atmosphere. The first process was reversible with no decomposition of the $YBaCo_4O_{7+\delta}$ phase [27]. The maximum oxygen content was obtained at temperatures lower than 500°C, achieving $\delta \approx 1.0$ and $\delta \approx 1.2$ in air and oxygen atmospheres, respectively [27,28]. The unique ability of the $YBaCo_4O_{7+\delta}$ phase to reversibly absorb and release oxygen makes it a possible candidate as an oxygen carrier that works at low temperatures in the CLAS system. The crystal structure consists of the three-dimensional network of corner-sharing $CoO_4$ tetrahedra. The corner-sharing $CoO_4$ framework allows oxygen modification in an atomic arrangement. As $YBaCo_4O_{7+\delta}$ decomposition takes place at a temperature above 600°C, improving that dynamical stability is a critical issue [29]. Doping in the Y or Co site is one of the positive choices to improve the stability. Ca, Tb-Lu and Zr can partially or completely substitute Y [28–35]. Fe, Al, Ga, Mn, Ni, Cu and Zn can partially substitute Co [36–38]. Kadota *et al.* [29] identified that the phase-decomposition temperature of $RBaCo_4O_{7+\delta}$ increased with decrease in the radius of the R ion. The decomposition temperature increased with increase in Sr doping concentration [35]. The phase-decomposition temperature of the 114 phase was increased by Al, Ga and Zn substituting for Co [33,35–37]. The increase was prominent, especially for the samples substituted by Al and Ga [35]. Räsänen *et al.* [36] reported that Al and Ga co-substituting for Co was more favourable than a single substitution of Al or Ga for improving thermal stability. However, Fe and Al co-substitution weakened the effects of Al substitution [31].

Very few works in the current literature focus on the kinetics of $YBaCo_4O_{7+\delta}$ oxygen carriers for CLAS applications. As is known, $YBaCo_4O_{7+\delta}$ shows a slower oxygen absorption rate and a faster oxygen desorption rate at lower temperatures [32,39]. For the application, the kinetics features are greatly impacted by the reactor size and the solid inventory. The reaction rate of $YBaCo_4O_{7+\delta}$ varies with different working parameters such as reaction temperature, conversion range, oxygen concentration and particle size [40–42]. Generally, the kinetics of gas–solid reactions is complex. However, for $YBaCo_4O_{7+\delta}$ oxygen carriers, the kinetic description of the process is relatively simple as there is no phase change. Indeed, the product of the gas–solid reaction is of a different solid phase from that of the solid reactant, the difference in density of the two solid phases imposing chemical constraints on the solid–solid interface [43,44]. As this surface area is a kinetic parameter for the gas–solid reaction, a phenomenological kinetic description of the process is often impossible. In the case of perovskite, the oxidation process involves physical adsorption on the surface and the oxygen vacancies are filled by oxygen ions migrating

from the bulk. The oxygen ions are involved in dissociative adsorption and chemical adsorption. The diffusion of oxygen ions is one of the processes which might control the rate of the oxidation reaction. The different adsorption steps and the possible surface migration of these adsorbed species to the reaction sites might also be rate-controlling [43]. In the case of the chemical reaction-controlled process, action there proceeds uniformly throughout the solid particles. In this case, different models need to be employed. The mechanism and kinetic parameters obtained here are quite vital when this material is used in the reactors.

# 2. Experimental section

## 2.1. Preparation of materials

Samples of $YBaCo_4O_{7+\delta}$, $Y_{0.95}Ti_{0.05}BaCo_4O_{7+\delta}$ and $Y_{0.5}Dy_{0.5}BaCo_4O_{7+\delta}$ were synthesized by a solid-state reaction. Mixed appropriate stoichiometric amounts of the starting materials, $Y_2O_3$, $TiO_2$, $Dy_2O_3$, $BaCO_3$ and $Co_3O_4$, were ground thoroughly and then calcined at 1000°C for 15 h. The calcined samples were reground and calcined at 1100°C for 30 h. After calcination, all the samples were ground with a mortar and sieved with a 400-mesh sieve (average particle size less than or equal to 37.5 µm) for experiments and kinetic analysis.

## 2.2. Characterization of materials

Phase composition was studied by a powder X-ray diffraction technique (Panalytical, PW 3040/60; X'Pert Pro system with Cu K$\alpha$ radiation). X-ray data were recorded with a step scan of 0.02° for 2$\theta$ between 10° and 70°, and the cell parameters were determined with JADE software. The microstructure of the synthesized samples was observed with scanning electron microscopy (SEM) on an ultra plus field emission scanning electron microscope. The oxygen absorption behaviour was observed with isothermal TG experiments in a thermogravimetric analyzer-TGA (STA409PC). During the TG experiment, a powder sample, with a mass of 10 mg, was heated to the target temperature (290, 310, 330 and 350°C) in a $N_2$ atmosphere to prevent the occurrence of oxygen absorption. Then the atmosphere was changed to an air flow of 40 ml $min^{-1}$, keeping the target temperature for 2 h to investigate the oxygen absorption behaviour. Before the kinetic experiments, the internal and external diffusion were eliminated by the experiments by varying the gas flow rate and the sample loading weight in the ranges of 20–40 ml $min^{-1}$ and 10–20 mg, respectively.

# 3. Results and discussion

## 3.1. Characterization

The phase composition of the $YBaCo_4O_{7+\delta}$, $Y_{0.95}Ti_{0.05}BaCo_4O_{7+\delta}$ and $Y_{0.5}Dy_{0.5}BaCo_4O_{7+\delta}$ samples is shown in figure 1. The cell parameters of the samples are refined from the data in space group $P6_3mc$, and the refined cell parameters are presented in table 1. By combining with the XRD patterns and refined cell parameters, the present samples are indexed to be of $YBaCo_4O_{7+\delta}$ structure. Typical SEM images of samples are shown in figure 2. It is seen that the samples consist of porous agglomerates of primary particles. The differences in morphology with different substituting ions of the oxygen carriers are very small.

The 114 phase oxygen carriers can absorb certain amounts of oxygen at different temperatures. The percentage change in mass $\Delta m$ (%) and total stoichiometric change ($\delta$) obtained at different oxidation temperatures are presented in table 2. The amount of oxygen absorption increases with increase in the oxidation temperature lower than 330°C. The amount of oxygen absorption obtained at 350°C is lower than that of the value obtained at 330 and 310°C. Furthermore, at a given oxidation temperature, the amount of oxygen absorption of Ti and Dy substituting samples is larger than that of the unsubstituted sample. Figure 3*a–c* shows the conversions of the $YBaCo_4O_{7+\delta}$, $Y_{0.95}Ti_{0.05}BaCo_4O_{7+\delta}$ and $Y_{0.5}Dy_{0.5}BaCo_4O_{7+\delta}$ oxygen carriers during oxidation reactions at different temperatures, respectively. As can be seen, the oxygen absorption rate of oxygen carriers increases with increase in the oxidation temperature. The oxygen carriers absorb oxygen completely within 70 min when the temperatures are 330 and 350°C. When the temperatures are 290 and 310°C, the saturation time of oxygen adsorption is approximately 100 min. The reason behind this may be that increase in oxidation temperature is conducive to the greater diffusion of oxygen ions.

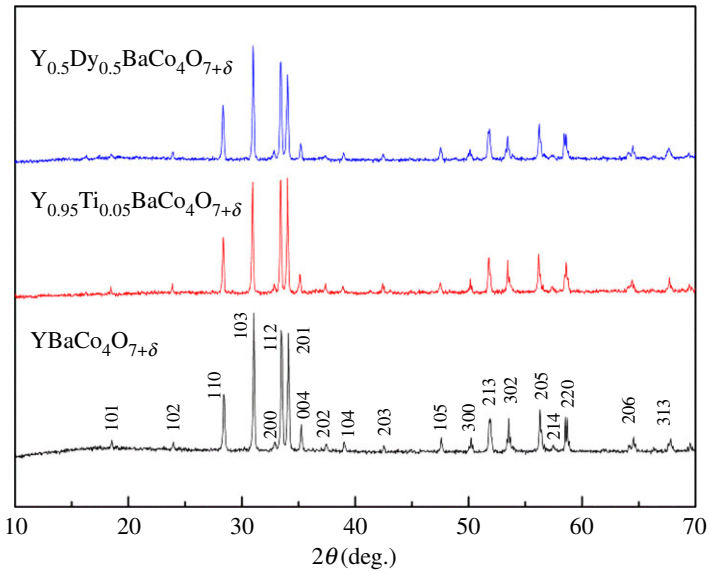


**Figure 1.** The XRD of the $YBaCo_4O_{7+\delta}$, $Y_{0.95}Ti_{0.05}BaCo_4O_{7+\delta}$ and $Y_{0.5}Dy_{0.5}BaCo_4O_{7+\delta}$ samples.

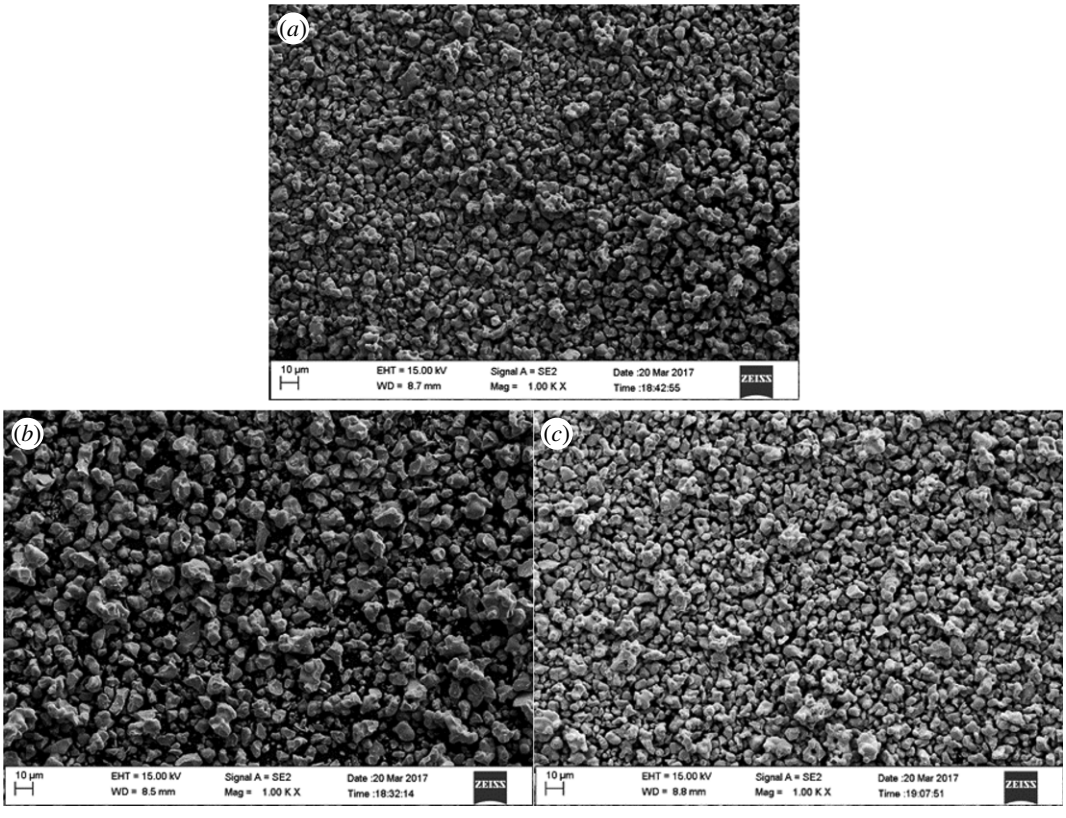


**Figure 2.** SEM images of the (*a*) $YBaCo_4O_{7+\delta}$, (*b*) $Y_{0.95}Ti_{0.05}BaCo_4O_{7+\delta}$ and (*c*) $Y_{0.5}Dy_{0.5}BaCo_4O_{7+\delta}$ samples.

**Table 1.** Refinement details for the samples.

| sample | *a* (Å) | *b* (Å) | *c* (Å) | *V* (Å$^3$) |
|---|---|---|---|---|
| $YBaCo_4O_{7+\delta}$ | 6.2983 | 6.2983 | 10.1728 | 349.4661 |
| $Y_{0.5}Dy_{0.5}BaCo_4O_{7+\delta}$ | 6.3076 | 6.3076 | 10.1953 | 351.2900 |
| $Y_{0.95}Ti_{0.05}BaCo_4O_{7+\delta}$ | 6.2969 | 6.2969 | 10.1725 | 349.3005 |

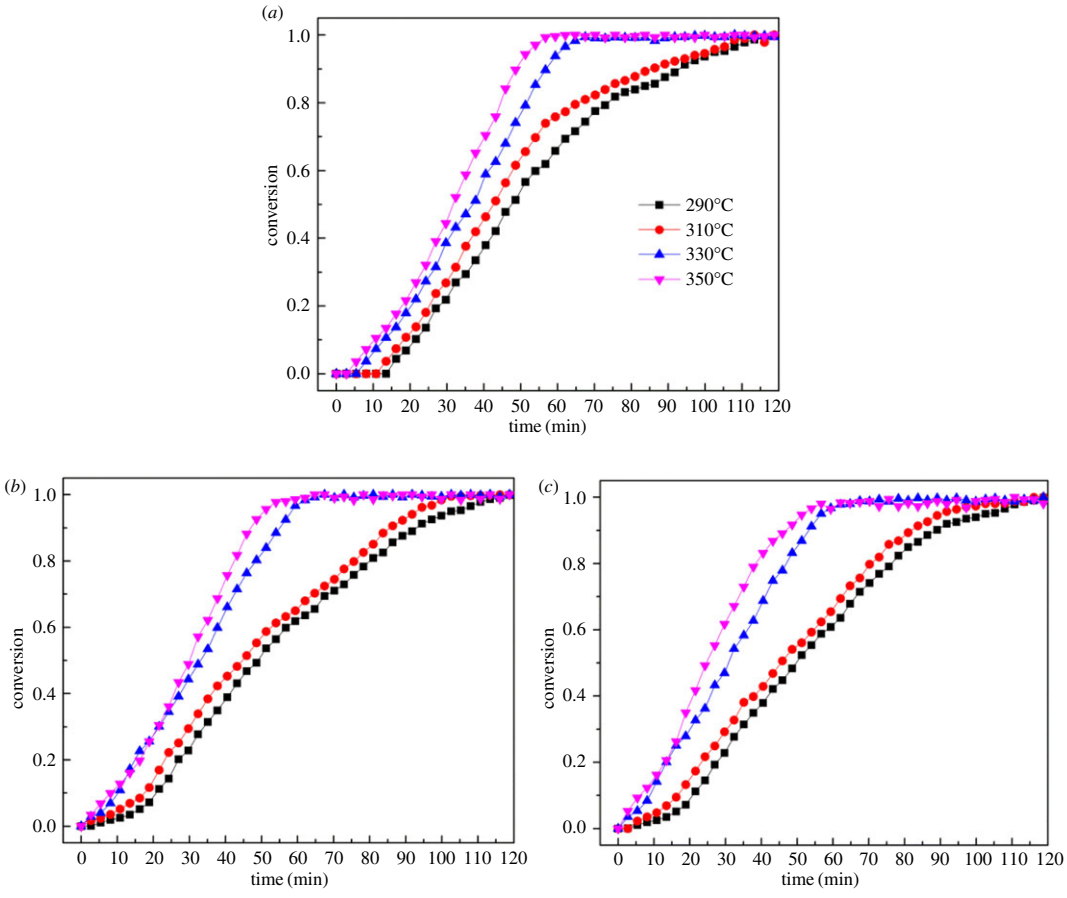


**Figure 3.** The conversion of oxidation in air atmosphere for the (*a*) $YBaCo_4O_{7+\delta}$, (*b*) $Y_{0.95}Ti_{0.05}BaCo_4O_{7+\delta}$ and (*c*) $Y_{0.5}Dy_{0.5}BaCo_4O_{7+\delta}$ samples.

**Table 2.** The mass change of the samples under different temperatures.

| | $YBaCo_4O_{7+\delta}$ | | | | $Y_{0.95}Ti_{0.05}BaCo_4O_{7+\delta}$ | | | | $Y_{0.5}Dy_{0.5}BaCo_4O_{7+\delta}$ | | | |
|---|---|---|---|---|---|---|---|---|---|---|---|---|
| | 290°C | 310°C | 330°C | 350°C | 290°C | 310°C | 330°C | 350°C | 290°C | 310°C | 330°C | 350°C |
| $\Delta m$/% | 1.982 | 2.211 | 2.244 | 2.123 | 2.011 | 2.341 | 2.376 | 2.209 | 1.897 | 2.289 | 2.315 | 2.237 |
| $\delta$ | 0.711 | 0.793 | 0.805 | 0.762 | 0.719 | 0.837 | 0.849 | 0.790 | 0.724 | 0.874 | 0.884 | 0.854 |

## 3.2. Kinetic models

The reaction rate of the process [45] can be written as follows:

$$k = \frac{d\alpha}{dt} = k(T)f(\alpha), \tag{3.1}$$

where $\alpha$ is the extent of conversion, $k(T)$ is the reaction rate content and $f(\alpha)$ is the kinetic model function. Equation (3.1) can be modified as follows:

$$\frac{d\alpha}{f(\alpha)} = k(T)dt. \tag{3.2}$$

Equation (3.2) can be transformed into equations (3.3*a*,*b*):

$$\int_0^{\alpha_1} \frac{d\alpha}{f(\alpha)} = G(\alpha) = \int_0^{t_1} k(T)dt \tag{3.3a}$$

$$G(\alpha) = k(T)t. \tag{3.3b}$$

**Table 3.** Kinetic mechanism functions used for describing oxidation kinetics of oxygen carriers.

| symbol | reaction model | $f(\alpha)$ | $g(\alpha)$ |
|---|---|---|---|
| R1 | zero-order | 1 | $\alpha$ |
| R2 | phase-boundary controlled reaction | $2(1-\alpha)^{1/2}$ | $[1-(1-\alpha)^{1/2}]$ |
| R3 | phase-boundary controlled reaction | $3(1-\alpha)^{2/3}$ | $[1-(1-\alpha)^{1/3}]$ |
| F3/2 | three-halves order | $(1-\alpha)^{3/2}$ | $2[(1-\alpha)^{-1/2}-1]$ |
| F2 | second-order | $(1-\alpha)^{2}$ | $(1-\alpha)^{-1}-1$ |
| F3 | third-order | $(1-\alpha)^{3}$ | $(1/2)[(1-\alpha)^{-2}-1]$ |
| A1/4 | Avrami-Erofeev ($n=1/4$) | $(1/4)(1-\alpha)[-\ln(1-\alpha)]^{-3}$ | $[-\ln(1-\alpha)]^{4}$ |
| A1/3 | Avrami-Erofeev ($n=1/3$) | $(1/3)(1-\alpha)[-\ln(1-\alpha)]^{-2}$ | $[-\ln(1-\alpha)]^{3}$ |
| A1/2 | Avrami-Erofeev ($n=1/2$) | $(1/2)(1-\alpha)[-\ln(1-\alpha)]^{-1}$ | $[-\ln(1-\alpha)]^{2}$ |
| A2/3 | Avrami-Erofeev ($n=2/3$) | $(2/3)(1-\alpha)[-\ln(1-\alpha)]^{-1/2}$ | $[-\ln(1-\alpha)]^{3/2}$ |
| A1 | Avrami-Erofeev ($n=1$) | $(1-\alpha)$ | $-\ln(1-\alpha)$ |
| A3/2 | Avrami-Erofeev ($n=3/2$) | $(3/2)(1-\alpha)[-\ln(1-\alpha)]^{1/3}$ | $[-\ln(1-\alpha)]^{2/3}$ |
| A2 | Avrami-Erofeev ($n=2$) | $2(1-\alpha)[-\ln(1-\alpha)]^{1/2}$ | $[-\ln(1-\alpha)]^{1/2}$ |
| A3 | Avrami-Erofeev ($n=3$) | $3(1-\alpha)[-\ln(1-\alpha)]^{2/3}$ | $[-\ln(1-\alpha)]^{1/3}$ |
| A4 | Avrami-Erofeev ($n=4$) | $4(1-\alpha)[-\ln(1-\alpha)]^{3/4}$ | $[-\ln(1-\alpha)]^{1/4}$ |

The plots of $G(\alpha)$ versus $t$ should be straight lines whose slope can be used to determine the reaction rate $k(T)$. The model showing the best linear fitting is chosen as the favoured model. The reaction models used for describing the oxidation process of oxygen carriers are presented in table 3 [41,42,45–49].

By linear fitting the mechanism functions against $t$ (parameters were estimated in the 0.1–0.90 conversion range), the linear correlation coefficient $R^2$ and the residual sum of squares (RSS) of each function can be obtained. Figure 4 shows the fitting linear curves $G(\alpha)$ versus $t$ under different oxidation temperatures.

Tables 4 and 5 list the $R^2$ and RSS values obtained by fitting functions, respectively. The discrimination among the models was based on the higher $R^2$ and lower RSS. The functions with the bigger $R^2$ and smaller RSS values are selected as the mechanism functions. For the $YBaCo_4O_{7+\delta}$ and $Y_{0.5}Dy_{0.5}BaCo_4O_{7+\delta}$ samples, given the $R^2$ and RSS values obtained, it was concluded that the A model and R better fitting were achieved with $n$ values of 4 and 1, respectively. For the $Y_{0.95}Ti_{0.05}BaCo_4O_{7+\delta}$ sample, it was concluded that the A model and R better fitting were achieved with $n$ values of 3 and 1, respectively. For the Avrami-Erofeev random nucleation and the nuclei growth model, the overall conversion of the oxygen absorption reaction is determined by the relative rates of nucleation, nuclei growth and nucleus formation [24,50–52]. Nucleation and crystal growth are a dynamic process which practically initiates the oxygen absorption reaction. Generally, for the unreacted shrinking-core model, the overall conversion of the oxygen absorption reaction is determined by the chemical process [24]. That is, the overall conversion of the reaction is dominated by the chemical reaction, not the diffusion process for the A models and R models. The determined models can be used to evaluate the reaction rate, apparent activation energy and pre-exponential factor of the oxygen absorption reaction. For the $YBaCo_4O_{7+\delta}$, $Y_{0.95}Ti_{0.05}BaCo_4O_{7+\delta}$ and $Y_{0.5}Dy_{0.5}BaCo_4O_{7+\delta}$ samples, the reaction rate constants are evaluated and presented in table 6.

From table 6, for the different mechanism functions and oxygen carriers, the reaction rate constant increases with increase in the reaction temperature, indicating that high temperature is propitious to the rate of oxygen adsorption. Low temperature may be one of the reasons accounting for the slow reaction rates shown in figure 3. Furthermore, the reaction rate (except for the reaction rate obtained at 290°C for the $Y_{0.95}Ti_{0.05}BaCo_4O_{7+\delta}$ sample) obtained by the A model is lower than that of the R model. After evaluating the reaction rate constant, the pre-exponential factor and apparent activation energy can be evaluated.

Along with the Arrhenius expression, the following is obtained:

$$k(T) = A\exp\left(-\frac{E}{RT}\right), \tag{3.4}$$

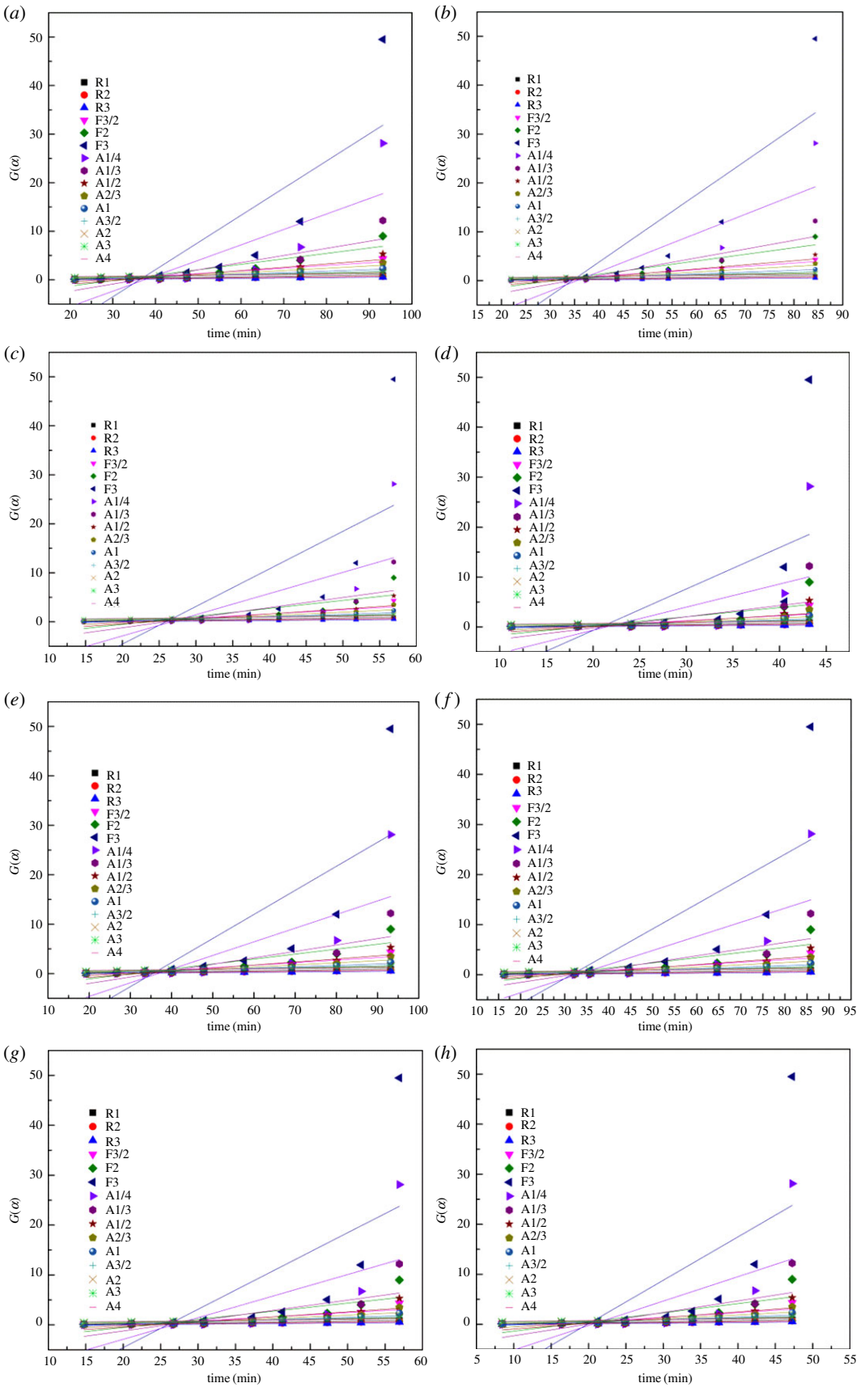


**Figure 4.** Trends of $G(\alpha)$ versus $t$ under different temperatures with common mechanism functions for the $YBaCo_4O_{7+\delta}$ oxidation process at (*a*) 290°C, (*b*) 310°C, (*c*) 330°C and (*d*) 350°C; for the $Y_{0.95}Ti_{0.05}BaCo_4O_{7+\delta}$ oxidation process at (*e*) 290°C, (*f*) 310°C, (*g*) 330°C and (*h*) 350°C; and for the $Y_{0.5}Dy_{0.5}BaCo_4O_{7+\delta}$ oxidation process at (*i*) 290°C, (*j*) 310°C, (*k*) 330°C and (*l*) 350°C.

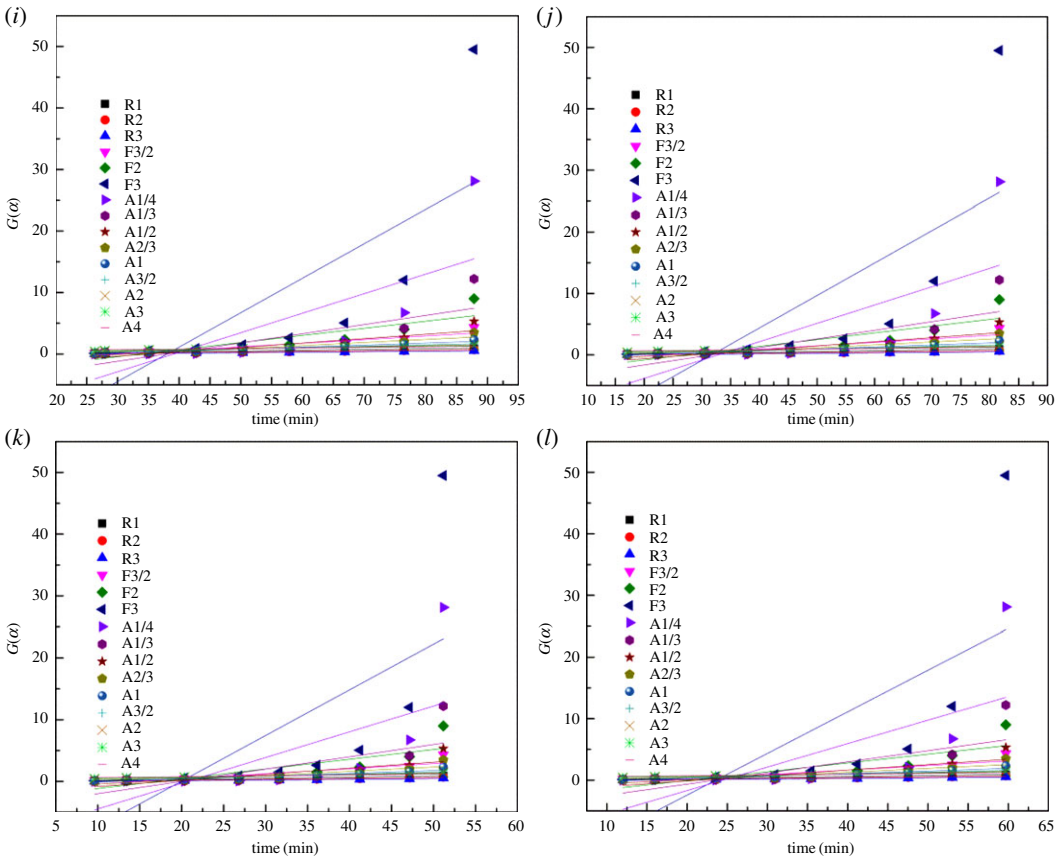


**Figure 4.** (*Continued*.)

where $A$ is the pre-exponential factor, $E$ is the apparent activation energy, $R$ is the gas constant and $T$ is the reaction temperature.

Along with the Arrhenius expression, the following form is obtained:

$$\ln k(T) = \ln A - \frac{E}{RT}, \tag{3.5}$$

where the $\ln k(T)$ has been evaluated above, the plots $\ln k(T)$ versus $1/T$ are straight lines whose slope and intercept can be used to evaluate the apparent activation energy and pre-exponential factor, respectively.

Figure 5 shows the plots $\ln k(T)$ versus $1/T$ as a function of different mechanism functions.

Table 7 lists the estimated apparent activation energy and pre-exponential factor as a function of reaction temperatures. The apparent activation energies obtained by the different mechanism functions remain close to constant levels for an oxygen carrier.

The activation energies for $Y_{0.5}Dy_{0.5}BaCo_4O_{7+\delta}$ oxidation are found to be lower than those for $YBaCo_4O_{7+\delta}$ and $Y_{0.95}Ti_{0.05}BaCo_4O_{7+\delta}$ oxidation, thus confirming the favourable effect of Dy on the oxidizability of the $YBaCo_4O_{7+\delta}$ oxygen carrier. This may be accounted for by the cell volume. The larger the cell volume, the easier is the absorption of oxygen. For an oxygen carrier, the pre-exponential factor obtained by the R model is larger than that of the A model.

For the purpose of further model discrimination between the A and R models, the A model is more favourable considering the higher unity of data values. In the case of the A model, the activation energies and the frequency factor remain close to constant levels at the different temperatures. Moreover, the activation energies with the R model vary in a much wider range. Thus, these results confirm the adequacy of the A model over the R model [24]. Thus, the nucleation and nuclei growth model is chosen as the most possible mechanism function.

The values of the established kinetic parameters, the apparent activation energies, the pre-exponential factors and the mechanism function were introduced into equation (3.1) and the differential equation was obtained to predict the oxygen carrier conversion of the oxidation process for different reaction time durations. The kinetic models are listed in table 8.

**Table 4.** The linear correlation coefficient $R^2$ of the mechanism models under different temperatures. The values in italics are the three largest values of $R^2$ obtained by fitting functions.

| | $YBaCo_4O_{7+\delta}$ | | | | | $Y_{0.95}Ti_{0.05}BaCo_4O_{7+\delta}$ | | | | | $Y_{0.5}Dy_{0.5}BaCo_4O_{7+\delta}$ | | | | |
|---|---|---|---|---|---|---|---|---|---|---|---|---|---|---|---|
| code | 290°C | 310°C | 330°C | 350°C | average | 290°C | 310°C | 330°C | 350°C | average | 290°C | 310°C | 330°C | 350°C | average |
| R1 | 0.9657 | 0.9388 | 0.9984 | 0.9548 | *0.9644* | 0.9842 | 0.9862 | 0.9984 | 0.9920 | *0.9902* | 0.9833 | 0.9959 | 0.9975 | 0.9855 | *0.9906* |
| R2 | 0.9962 | 0.9837 | 0.9729 | 0.8833 | 0.9590 | 0.9984 | 0.9943 | 0.9729 | 0.9599 | 0.9814 | 0.9961 | 0.9916 | 0.9773 | 0.9799 | 0.9862 |
| R3 | 0.9978 | 0.9913 | 0.9542 | 0.8501 | 0.9484 | 0.9932 | 0.9868 | 0.9942 | 0.9400 | 0.9786 | 0.9903 | 0.9801 | 0.9605 | 0.9692 | 0.9750 |
| F3/2 | 0.9260 | 0.9518 | 0.7883 | 0.6351 | 0.8253 | 0.8826 | 0.8648 | 0.7883 | 0.7740 | 0.8274 | 0.8769 | 0.8436 | 0.8040 | 0.8438 | 0.8421 |
| F2 | 0.8358 | 0.8773 | 0.6330 | 0.5040 | 0.7125 | 0.7731 | 0.7505 | 0.6630 | 0.6521 | 0.7097 | 0.7667 | 0.7270 | 0.6824 | 0.7359 | 0.7280 |
| F3 | 0.6635 | 0.7203 | 0.4680 | 0.3261 | 0.5445 | 0.5812 | 0.5546 | 0.4689 | 0.4648 | 0.5174 | 0.5749 | 0.5348 | 0.4905 | 0.5554 | 0.5389 |
| A1/4 | 0.6446 | 0.7028 | 0.4482 | 0.3047 | 0.5251 | 0.5625 | 0.5362 | 0.4482 | 0.4439 | 0.4977 | 0.5558 | 0.5143 | 0.4699 | 0.5348 | 0.5187 |
| A1/3 | 0.7314 | 0.7834 | 0.5392 | 0.3820 | 0.6090 | 0.6579 | 0.6331 | 0.5392 | 0.5304 | 0.5902 | 0.6507 | 0.6068 | 0.5601 | 0.6209 | 0.6092 |
| A1/2 | 0.8560 | 0.8930 | 0.6890 | 0.5246 | 0.7406 | 0.8013 | 0.7803 | 0.6890 | 0.6741 | 0.7362 | 0.7948 | 0.7530 | 0.7071 | 0.7555 | 0.7526 |
| A2/3 | 0.9270 | 0.9508 | 0.7910 | 0.6346 | 0.8258 | 0.8877 | 0.8705 | 0.7910 | 0.7740 | 0.8308 | 0.9896 | 0.8471 | 0.8061 | 0.8429 | 0.8714 |
| A1 | 0.9851 | 0.9915 | 0.9006 | 0.7713 | 0.9121 | 0.9652 | 0.9540 | 0.9006 | 0.8852 | 0.9263 | 0.9611 | 0.9401 | 0.9110 | 0.9324 | 0.9362 |
| A3/2 | 0.9994 | 0.9928 | 0.9619 | 0.8470 | 0.9503 | 0.9937 | 0.9877 | 0.9619 | 0.9517 | 0.9738 | 0.9896 | 0.9835 | 0.9676 | 0.9788 | 0.9799 |
| A2 | 0.9939 | 0.9809 | 0.9827 | 0.7957 | 0.9383 | 0.9900 | 0.9919 | 0.9827 | 0.9767 | 0.9853 | 0.9802 | 0.9934 | 0.9856 | 0.9925 | 0.9879 |
| A3 | 0.9778 | 0.9589 | 0.9937 | 0.9365 | *0.9667* | 0.9852 | 0.9850 | 0.9937 | 0.9931 | *0.9893* | 0.9796 | 0.9924 | 0.9935 | 0.9971 | *0.9907* |
| A4 | 0.9654 | 0.9491 | 0.9949 | 0.9527 | *0.9642* | 0.9757 | 0.9769 | 0.9949 | 0.9974 | *0.9862* | 0.9694 | 0.9933 | 0.9939 | 0.9957 | *0.9881* |

**Table 5.** The residual sum of squares RSS of the mechanism models under different temperatures. The values in italics are the RSS values obtained by fitting three functions with the largest values of $R^2$.

| | $YBaCo_4O_{7+\delta}$ | | | | | $Y_{0.95}Ti_{0.05}BaCo_4O_{7+\delta}$ | | | | | $Y_{0.5}Dy_{0.5}BaCo_4O_{7+\delta}$ | | | | |
|---|---|---|---|---|---|---|---|---|---|---|---|---|---|---|---|
| code | 290°C | 310°C | 330°C | 350°C | average | 290°C | 310°C | 330°C | 350°C | average | 290°C | 310°C | 330°C | 350°C | average |
| R1 | 0.0206 | 0.0367 | 0.0010 | 0.0271 | *0.0214* | 0.0095 | 0.0083 | 0.0097 | 0.0053 | *0.0082* | 0.0100 | 0.0025 | 0.0025 | 0.0027 | *0.0044* |
| R2 | 0.0014 | 0.0058 | 0.0097 | 0.0419 | 0.0147 | 0.0006 | 0.0020 | 0.0097 | 0.0143 | 0.0067 | 0.0014 | 0.0030 | 0.0082 | 0.0072 | 0.0050 |
| R3 | 0.0005 | 0.0019 | 0.0102 | 0.0333 | 0.0115 | 0.0015 | 0.0029 | 11.4687 | 0.0133 | 2.8716 | 0.0021 | 0.0044 | 0.0088 | 0.0068 | 0.0055 |
| F3/2 | 1.0945 | 0.7120 | 3.1300 | 4.3932 | 2.3324 | 1.7352 | 1.9987 | 3.1300 | 3.3400 | 2.5509 | 1.8195 | 2.3126 | 2.8974 | 2.3086 | 2.3345 |
| F2 | 10.683 | 7.983 | 21.921 | 32.264 | 18.2128 | 14.7584 | 16.230 | 21.921 | 22.628 | 18.884 | 15.180 | 17.762 | 20.661 | 17.181 | 17.696 |
| F3 | 688.64 | 572.29 | 1086.69 | 1379.06 | 931.670 | 857.06 | 911.45 | 1086.69 | 1095.18 | 987.59 | 869.82 | 951.87 | 1042.48 | 909.84 | 943.50 |
| A1/4 | 241.74 | 202.18 | 375.31 | 472.94 | 323.04 | 297.61 | 315.47 | 375.31 | 378.25 | 341.66 | 302.14 | 330.40 | 360.58 | 316.42 | 327.39 |
| A1/3 | 34.464 | 27.789 | 59.124 | 79.289 | 50.166 | 43.888 | 47.079 | 59.124 | 60.248 | 52.585 | 44.810 | 50.447 | 56.438 | 48.640 | 50.08 |
| A1/2 | 3.4898 | 2.5931 | 7.5353 | 11.5183 | 6.2842 | 4.1832 | 5.3235 | 7.5353 | 7.8953 | 6.2342 | 4.9724 | 5.9834 | 7.0962 | 5.9233 | 5.9938 |
| A2/3 | 0.7566 | 0.5093 | 2.1652 | 3.7844 | 1.8039 | 1.1636 | 1.3416 | 2.1652 | 2.3407 | 1.7528 | 1.2197 | 1.5838 | 2.0081 | 1.6278 | 1.6099 |
| A1 | 0.0617 | 0.0351 | 0.4113 | 0.9465 | 0.3637 | 0.1439 | 0.1902 | 0.4113 | 0.4748 | 0.3051 | 0.1610 | 0.2481 | 0.3685 | 0.2798 | 0.2644 |
| A3/2 | 0.0011 | 0.0141 | 0.0745 | 0.2617 | 0.0879 | 0.0123 | 0.0240 | 0.0745 | 0.0943 | 0.0513 | 0.0203 | 0.0322 | 0.0633 | 0.0416 | 0.0394 |
| A2 | 0.0073 | 0.0227 | 0.0206 | 0.1088 | 0.0399 | 0.0059 | 0.0097 | 0.0206 | 0.0276 | 0.0159 | 0.0115 | 0.0079 | 0.0172 | 0.0090 | 0.0114 |
| A3 | 0.0313 | 0.0245 | 0.0076 | 0.0332 | *0.0242* | 0.0089 | 0.0090 | 0.0038 | 0.0041 | *0.0065* | 0.0122 | 0.0046 | 0.0039 | 0.0017 | *0.0056* |
| A4 | 0.0125 | 0.0203 | 0.0019 | 0.0150 | *0.0124* | 0.0088 | 0.0084 | 0.0019 | 9.5628 | *2.3955* | 0.0111 | 0.0046 | 0.0026 | 0.0016 | *0.0048* |

**Table 6.** The reaction rate constants of the determined mechanism models under different temperatures.

| | $YBaCo_4O_{7+\delta}$ | | | | | $Y_{0.95}Ti_{0.05}BaCo_4O_{7+\delta}$ | | | | | $Y_{0.5}Dy_{0.5}BaCo_4O_{7+\delta}$ | | | |
|---|---|---|---|---|---|---|---|---|---|---|---|---|---|---|
| code | 290°C | 310°C | 330°C | 350°C | code | 290°C | 310°C | 330°C | 350°C | code | 290°C | 310°C | 330°C | 350°C |
| A4 | 0.00813 | 0.01050 | 0.01488 | 0.01895 | A3 | 0.00933 | 0.01130 | 0.01727 | 0.02165 | A4 | 0.00744 | 0.00956 | 0.01452 | 0.01677 |
| R1 | 0.01037 | 0.01348 | 0.01918 | 0.02434 | R1 | 0.00929 | 0.01134 | 0.01918 | 0.02168 | R1 | 0.00949 | 0.01236 | 0.01878 | 0.02148 |

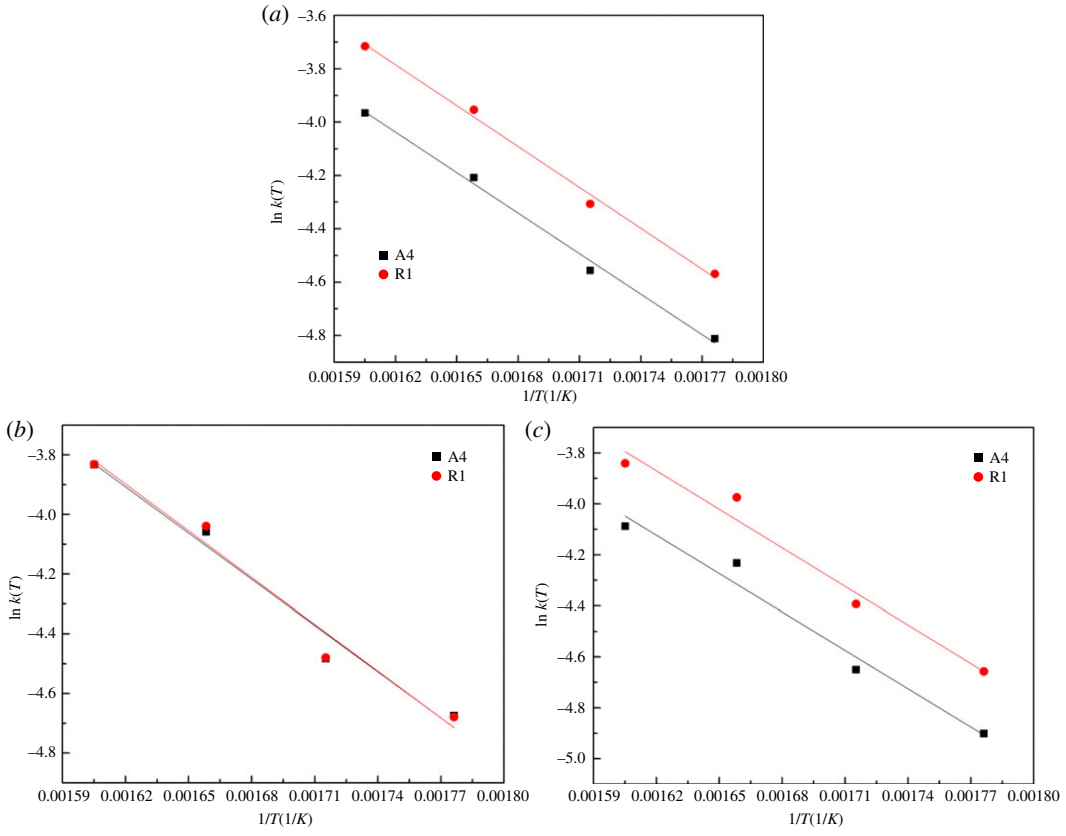


**Figure 5.** The plots of $\ln k(T)$ versus $1/T$ for different mechanism functions for the (*a*) $YBaCo_4O_{7+\delta}$, (*b*) $Y_{0.95}Ti_{0.05}BaCo_4O_{7+\delta}$ and (*c*) $Y_{0.5}Dy_{0.5}BaCo_4O_{7+\delta}$ samples.

**Table 7.** The apparent activation energy and pre-exponential factor of the obtained function for the oxidation process of oxygen carriers.

| oxygen carrier | code | $R^2$ | RSS | slope | intercept | $E$ (J mol$^{-1}$) | $A$ (min$^{-1}$) |
|---|---|---|---|---|---|---|---|
| $YBaCo_4O_{7+\delta}$ | A4 | 0.9948 | 0.00814 | −4526.9800 | 3.2842 | 42078.5466 | 64.1677 |
| | R1 | 0.9949 | 0.00853 | −4522.3570 | 3.5280 | 42649.0491 | 92.2406 |
| $Y_{0.95}Ti_{0.05}BaCo_4O_{7+\delta}$ | A3 | 0.9759 | 0.00977 | −5165.2298 | 4.0446 | 42943.7206 | 84.8258 |
| | R1 | 0.9739 | 0.01296 | −5228.2237 | 4.5719 | 43467.4518 | 96.7277 |
| $Y_{0.5}Dy_{0.5}BaCo_4O_{7+\delta}$ | A4 | 0.9739 | 0.01117 | −5016.9196 | 4.0446 | 41710.6696 | 57.0901 |
| | R1 | 0.9723 | 0.01234 | −5040.2659 | 4.2952 | 41904.7707 | 73.3469 |

**Table 8.** The kinetic models of different oxygen carriers.

| oxygen carrier | code | kinetic model |
|---|---|---|
| $YBaCo_4O_{7+\delta}$ | A4 | $\frac{d\alpha}{dt} = 256.671 \exp\left(-\frac{42078.547}{RT}\right)(1-\alpha)[-\ln(1-\alpha)]^{3/4}$ |
| $Y_{0.95}Ti_{0.05}BaCo_4O_{7+\delta}$ | A3 | $\frac{d\alpha}{dt} = 254.477 \exp\left(-\frac{42943.721}{RT}\right)(1-\alpha)[-\ln(1-\alpha)]^{2/3}$ |
| $Y_{0.5}Dy_{0.5}BaCo_4O_{7+\delta}$ | A4 | $\frac{d\alpha}{dt} = 228.360 \exp\left(-\frac{41710.670}{RT}\right)(1-\alpha)[-\ln(1-\alpha)]^{3/4}$ |

# 4. Conclusion

In this work, kinetic behaviour of the oxidation process for the $YBaCo_4O_{7+\delta}$, $Y_{0.95}Ti_{0.05}BaCo_4O_{7+\delta}$ and $Y_{0.5}Dy_{0.5}BaCo_4O_{7+\delta}$ oxygen carriers for CLAS operations was investigated for the temperature range of 290–350°C. The oxidation rate was found to increase gradually with increase in reaction temperature. It has been found that the A model provides a better description of the oxidation, indicating that the oxygen absorption process is rate-determined by nucleation and nuclei growth. The activation energies of the oxidation process obtained by the A model were determined as 42.079 kJ $mol^{-1}$, 42.944 kJ $mol^{-1}$ and 41.711 kJ $mol^{-1}$ for the $YBaCo_4O_{7+\delta}$, $Y_{0.95}Ti_{0.05}BaCo_4O_{7+\delta}$ and $Y_{0.5}Dy_{0.5}BaCo_4O_{7+\delta}$ oxygen carriers, respectively. The distributed activation energy of $Y_{0.5}Dy_{0.5}BaCo_4O_{7+\delta}$ is lower than that of $YBaCo_4O_{7+\delta}$, which corroborates the favourable effect of the substitution of Dy on the oxidizability of the oxygen carrier. The pre-exponential factors of the oxidation process obtained by the A model were determined as 64.168 $min^{-1}$, 84.826 $min^{-1}$ and 57.090 $min^{-1}$ for the $YBaCo_4O_{7+\delta}$, $Y_{0.95}Ti_{0.05}BaCo_4O_{7+\delta}$ and $Y_{0.5}Dy_{0.5}BaCo_4O_{7+\delta}$ oxygen carriers, respectively. The kinetic model was obtained to predict the oxygen carrier conversion of oxygen absorption for different time durations.

Data accessibility. The data have been uploaded as the electronic supplementary file.

Authors' contributions. L.H. and Q.Y. designed the study. L.H. and K.W. prepared the samples and conducted the experiments. L.H. and Q.Q. analysed the data. L.H., M.W. and F.Y. interpreted the results and wrote the manuscript.

Competing interests. We declare we have no competing interests.

Funding. This study was financially supported by the National Natural Science Foundation of China (grant nos. 51576035 and 51604078) and Fundamental Research Funds for the Central Universities (grant no. N162504012) and Post-Doctoral Science Foundation (grant nos. 2017M610185 and 20170101).

Acknowledgements. We are grateful to Huaqing Xie and Haiyang Yu who provided the comments that reduced the grammatical and spelling errors.

# References

1. Moghtaderi B, Song H. 2010 Reduction properties of physically mixed metallic oxide oxygen carriers in chemical looping combustion. *Energy Fuels* **24**, 5359–5368. (doi:10.1021/ef1006963)
2. Song H, Shah K, Doroodchi E, Moghtaderi B. 2014 Development of a Cu-Mg-based oxygen carrier with $SiO_2$ as a support for chemical looping air separation. *Energy Fuels* **28**, 163–172. (doi:10.1021/ef401485p)
3. Moghtaderi B. 2010 Application of chemical looping concept for air separation at high temperatures. *Energy Fuels* **24**, 190–198. (doi:10.1021/ef900553j)
4. Song H, Shah K, Doroodchi E, Wall T, Moghtaderi B. 2014 Reactivity of $Al_2O_3$ or $SiO_2$ supported Cu, Mn, and Co-oxygen carriers for chemical looping air separation. *Energy Fuels* **28**, 1284–1294. (doi:10.1021/ef402268t)
5. Wang K, Yu QB, Qin Q. 2013 The thermodynamic method for selecting oxygen carriers used for chemical looping air separation. *J. Therm. Anal. Calorim.* **112**, 747–753. (doi:10.1007/s10973-012-2596-8)
6. Shulman A, Cleverstam E, Mattisson T, Lyngfelt A. 2009 Manganese/iron, manganese/nickel, and manganese/silicon oxides used in chemical-looping with oxygen uncoupling for combustion methane. *Energy Fuels* **23**, 5269–5275. (doi:10.1021/ef9005466)
7. Wang K, Yu QB, Xie HQ, Qin Q. 2013 Performance and apparent redox kinetic of a Cu-based oxygen carrier for chemical looping oxygen production. *Funct. Mater. Lett.* **6**, 1–5.
8. Wang K, Yu QB, Qin Q, Zuo ZL. 2015 Study of the sorption property of copper oxygen carrier used for chemical looping air separation. *J. Therm. Anal. Calorim.* **120**, 1627–1633. (doi:10.1007/s10973-015-4509-0)
9. Wang K, Yu QB, Qin Q. 2013 Reduction kinetics of Cu-based oxygen carriers for chemical looping air separation. *Energy Fuels* **27**, 5466–5474. (doi:10.1021/ef401241r)
10. Ishida M, Yamamoto M, Ohba T. 2002 Experimental results of chemical-looping combustion with $NiO/NiAl_2O_4$ particle circulation at 1200°C. *Energy Convers. Manage.* **43**, 1469–1478. (doi:10.1016/S0196-8904(02)00029-8)
11. Mattisson T, Lyngfelt A, Leion H. 2009 Chemical-looping with oxygen uncoupling for combustion of solid fuels. *Int. J. Greenhouse Gas Control* **3**, 11–19. (doi:10.1016/j.ijggc.2008.06.002)
12. Arjmand M, Keller M, Leion H, Mattisson T, Lyngfelt A. 2012 Oxygen release and oxidation rates of $MgAl_2O_4$-supported CuO oxygen carrier for chemical-looping combustion with oxygen uncoupling (CLOU). *Energy Fuels* **26**, 6528–6539. (doi:10.1021/ef3010064)
13. Wang K, Yu QB, Qin Q. 2015 Analysis of oxygen releasing rate of Cu-based oxygen carrier in $N_2$–$O_2$ atmosphere. *J. Therm. Anal. Calorim.* **119**, 2221–2227. (doi:10.1007/s10973-014-4343-9)
14. Magnus R, Henrik L, Tobias M, Anders L. 2014 Combined oxides as oxygen-carrier material for chemical-looping with oxygen uncoupling. *Appl. Energy* **113**, 1924–1932. (doi:10.1016/j.apenergy.2013.06.016)
15. Zhao K, He F, Huang Z, Wei GQ, Zheng AQ, Li HB, Zhao ZL. 2017 Perovskite-type $LaFe_{1-x}Mn_xO_3$ ($x = 0, 0.3, 0.5, 0.7, 1.0$) oxygen carriers for chemical-looping steam methane reforming: oxidation activity and resistance to carbon formation. *Korean J. Chem. Eng.* **34**, 1651–1660. (doi:10.1007/s11814-016-0329-6)
16. Leonidov IA, Konstantinova EI, Patrakeev MV, Markov AA, Kozhevnikov VL. 2017 Electrical conductivity and carrier mobility in $Ca_{1-x}Pr_xMnO_{3-\delta}$ manganites. *Inorg. Mater.* **53**, 589–594. (doi:10.1134/S0020168517060103)
17. Adánez J, de Diego LF, García-Labiano F, Gayán P, Abad A. 2004 Selection of oxygen carriers for chemical-looping combustion. *Energy Fuels* **18**, 371–377. (doi:10.1021/ef0301452)
18. Abad A, Adaez-Rubio I, Gaya P, Garc-Labiano F, de Diego LF, Adaez J. 2012 Demonstration of chemical-looping with oxygen uncoupling (CLOU) process in a 1.5 kW th continuously operating unit using a Cu-based oxygen carrier. *Int. J. Greenhouse Gas Control* **6**, 189–200. (doi:10.1016/j.ijggc.2011.10.016)
19. Wang K, Luan WP, Yu QB, Qin Q. 2018 The reduction kinetic of the combined Cu-based oxygen carrier used for chemical looping gasification technology. In *The Minerals, Metals & Materials Society Ann. Meeting & Exhibition*, *Phoenix, USA*, *2018*, pp. 89–97. Cham, Switzerland: Springer.
20. Wang BW, Li HY, Ding N, Shen QW, Zhao HB, Zheng CG. 2018 Chemical looping combustion characteristics of coal with $Fe_2O_3$ oxygen carrier. *J. Therm. Anal. Calorim.* **132**, 17–27. (doi:10.1007/s10973-017-6775-5)
21. Whitty K, Clayton C. 2012 Measurement and modeling of kinetics for copper-based chemical looping with oxygen uncoupling. In *Proc. 2nd Int. Conf. on Chemical Looping*, *Darmstadt, Germany*, *2012*, pp. 1–10. Amsterdam, The Netherlands: Elsevier.

22. Hossain MM. 2017 Solid-state kinetics of reduction of NiO/Ce-$\gamma$ $Al_2O_3$ oxygen carriers for chemical-looping combustion. *Arab. J. Sci. Eng.* **43**, 2281–2290. (doi:10.1007/s13369-017-2706-9)
23. Zhu J, Wang W, Lian SJ, Hua XN, Xia Z. 2017 Stepwise reduction kinetics of iron-based oxygen carriers by $CO/CO_2$ mixture gases for chemical looping hydrogen generation. *J. Mater. Cycles Waste Manage.* **19**, 453–462. (doi:10.1007/s10163-015-0443-2)
24. Hossain MM, de Lasa HI. 2010 Reduction and oxidation kinetics of Co-Ni/$Al_2O_3$ oxygen carrier involved in a chemical-looping combustion cycles. *Chem. Eng. Sci.* **65**, 98–106. (doi:10.1016/j.ces.2009.01.059)
25. Li F, Zeng L, Velazquez-Vargas LG, Yoscovits Z, Fan L. 2010 Syngas chemical looping gasification process: bench-scale studies and reactor simulations. *AIChE J.* **56**, 2186–2199. (doi:10.1002/aic.12093)
26. Valldor M, Andersson M. 2002 The structure of the new compound $YBaCo_4O_7$ with a magnetic feature. *Solid State Sci.* **4**, 923–931. (doi:10.1016/S1293-2558(02)01342-0)
27. Karppinen M, Yanauchi H, Otani S, Fujita T, Motohashi T, Huang YH, ValkeapÓŞÓŞ M, Fjellvåg H. 2006 Oxygen nonstoichiometry in $YBaCo_4O_7$: large low-temperature oxygen absorption/desorption capability. *Chem. Mater.* **18**, 490–494. (doi:10.1021/cm0523081)
28. Motohashi T, Kadita S, Fjellvag H, Karppinen M, Yamauchi H. 2008 Uncommon oxygen intake/release capability of layered cobalt oxides $REBaCo_4O_{7+\delta}$: novel oxygen-storage materials. *Mater. Sci. Eng. B* **148**, 196–198. (doi:10.1016/j.mseb.2007.09.052)
29. Kadota S, Kappinen M, Motohashi T, Yamauchi H. 2008 R-site substitution effect on the oxygen-storage capability of $RBaCo_4O_{7+\delta}$. *Chem. Mater.* **20**, 6378–6381. (doi:10.1021/cm801412q)
30. Kozeeva LP, Kameneva MY, Lavrov AN, Podberezskaya NV. 2013 Synthesis and oxygen behavior of $RBaCo_4O_{7+\delta}$ (R = Y, Dy-Lu). *Inorg. Mater.* **49**, 626–631. (doi:10.1134/S0020168513060058)
31. Wang S, Hao HS, Zhu BF, Jia JF, Hu X. 2008 Modifying the oxygen adsorption properties of $YBaCo_4O_7$ by Ca, Al, and Fe doping. *J. Mater. Sci.* **43**, 5385–5389. (doi:10.1007/s10853-008-2806-8)
32. Hao HS, He QL, Cheng YG, Zhao LM. 2009 Oxygen adsorption/desorption behavior of $YBaCo_4O_{7+\delta}$ and its application to oxygen removal from nitrogen. *J. Rare Earth* **27**, 815–818. (doi:10.1016/S1002-0721(08)60341-5)
33. Zhang SM. 2011 Study on the oxygen adsorption/desorption properties of doped-$YBaCo_4O_{7+\delta}$ and its oxygen permeation ability. MA Dissertation, China, ZhengZhou University.
34. Guo LJ. 2005 Study on the oxygen adsorption/desorption properties of $YBaCo_4O_{7+\delta}$. MA Dissertation, China, ZhengZhou University.
35. Parkkima O, Yamauchi H, Karppinen M. 2013 Oxygen storage capacity and phase stability of variously substituted $YBaCo_4O_{7+\delta}$. *Chem. Mater.* **25**, 599–604. (doi:10.1021/cm3038729)
36. Räsänen S, Motohashi T, Yamauchi H, Kappinen M. 2012 Ga-for-Co substitution in $YBaCo_4O_{7+\delta}$: effect on high-temperature stability and oxygen-storage capacity. *Solid State Ionics* **208**, 31–35. (doi:10.1016/j.ssi.2011.11.028)
37. Komiyama T, Motohashi T, Masubuchi Y, Kikkawa S. 2010 Synthesis, thermal stability, and oxygen intake/release characteristic of $YBa(Co_{1-x}Al_x)_4O_{7+\delta}$. *Mater. Res. Bull.* **45**, 1527–1532. (doi:10.1016/j.materresbull.2010.06.031)
38. Jung-Hyun K, Arumugam M. 2010 Low thermal expansion $RBa(Co,M)_4O_7$ cathode materials based on tetrahedral-site cobalt ions for solid oxide fuel cells. *Chem. Mater.* **22**, 822–831. (doi:10.1021/cm9015244)
39. Rui ZB, Ding JJ, Li F, Lin YS, Li YD. 2012 $YBaCo_4O_{7+\delta}$ sorbent for oxygen-enriched carbon dioxide stream production at a low-temperature. *Fuel* **94**, 191–196. (doi:10.1016/j.fuel.2011.10.073)
40. de Diego LF, García-Labiano F, Adánez J, Gayán P, Abad A, Corbella BM, María PJ. 2004 Development of Cu-based oxygen carriers for chemical-looping combustion. *Fuel* **83,** 1749–1757. (doi:10.1016/j.fuel.2004.03.003)
41. Jin H, Okamoto T, Ishida M. 1998 Development of a novel chemical-looping combustion: synthesis of a looping material with a double metal oxide of CoO-NiO. *Energy Fuels* **12**, 1272–1277. (doi:10.1021/ef980080g)
42. Jin H, Okamoto T, Ishida M. 2005 Development of a novel chemical-looping combustion: synthesis of a solid looping material of NiO/$NiAl_2O_4$. *Ind. Eng. Chem. Res.* **38**, 126–132. (doi:10.1021/ie980326 5)
43. Delmon B. 1969 *Introduction à la Cinet´ique Het´erogen'e*, p. 256. Paris: Technip.
44. Sarshar Z, Kaliaguine S. 2013 Reduction kinetics of perovskite-based oxygen carriers for chemical looping combustion. *Ind. Eng. Chem. Res.* **52**, 6946–6955. (doi:10.1021/ie400766b)
45. Vyazovkin S, Wight CA. 1999 Model-free and model-fitting approaches to kinetic analysis of isothermal and nonisothermal data. *Thermachim. Acta* **340–341**, 53–68. (doi:10.1016/S0040-6031(99)00253-1)
46. Halikia I, Neou-Syngouna P, Kolitsa D. 1998 Isothermal kinetic analysis of the thermal decomposition of magnesium hydroxide using thermogravimetric data. *Thermochim. Acta* **320**, 75–88. (doi:10.1016/S0040-6031(98)00413-4)
47. Perkins C, Lichty P, Weimer AW. 2007 Determination of aerosol kinetics of thermal ZnO dissociation by thermogravimetry. *Chem. Eng. Sci.* **62**, 5952–5962. (doi:10.1016/j.ces.2007.06.039)
48. Kubaschewsk O, Alcock CB. 1979 *Metallurgical thermochemistry*, pp. 1. New York, NY: Pergamon Press.
49. Pineau A, Kanari N, Gaballah I. 2006 Kinetics of reduction of iron oxides by H2: Part I: low temperature reduction of hematite. *Thermochim. Acta* **447**, 89–100. (doi:10.1016/j.tca.2005.10.004)
50. Brown ME, Dollimore D, Galwey AK. 1980 *Reactions in the solid state in comprehensive chemical kinetics*, pp. 41–113. Amsterdam, Netherlands: Elsevier Science.
51. Hossain MM, Quddus MR, de Lasa HI. 2010 Reduction kinetics of La modified NiO/La-$\gamma$ $Al_2O_3$ oxygen carrier for chemical-looping combustion. *Ind. Eng. Chem. Res.* **49**, 11 009–11 017. (doi:10.1021/ie100424w)
52. Hossain MM, de Lasa HI. 2007 Chemical-looping combustion (CLC) for inherent $CO_2$ separations—a review. *Chem. Eng. Sci.* **63**, 4433–4451. (doi:10.1016/j.ces.2008.05.028)